

# The Ultraviolet Spectrum and Physical Properties of the Mass Donor Star in HD 226868 = Cygnus X-1<sup>1</sup>

S. M. Caballero-Nieves<sup>2</sup>, D. R. Gies<sup>2,3</sup>, C. T. Bolton<sup>4</sup>, P. Hadrava<sup>5</sup>, A. Herrero<sup>6</sup>, T. C. Hillwig<sup>3,7</sup>, S. B. Howell<sup>8</sup>, W. Huang<sup>3,9</sup>, L. Kaper<sup>10</sup>, P. Koubský<sup>5</sup>, and M. V. McSwain<sup>11</sup>

## ABSTRACT

---

<sup>1</sup>Based on observations with the NASA/ESA Hubble Space Telescope obtained at the Space Telescope Science Institute, which is operated by the Association of Universities for Research in Astronomy, Incorporated, under NASA contract NAS5-26555. These observations are associated with programs GO-9646 and GO-9840.

<sup>2</sup>Center for High Angular Resolution Astronomy, Department of Physics and Astronomy, Georgia State University, P. O. Box 4106, Atlanta, GA 30302-4106; scaballero@chara.gsu.edu, gies@chara.gsu.edu

<sup>3</sup>Visiting Astronomer, Kitt Peak National Observatory, National Optical Astronomy Observatory, operated by the Association of Universities for Research in Astronomy, Inc., under contract with the National Science Foundation.

<sup>4</sup>Department of Astronomy and Astrophysics, University of Toronto, 50 St. George Street, Room 101, Toronto, Ontario, Canada M5S 3H4; bolton@astro.utoronto.ca

<sup>5</sup>Astronomical Institute, Academy of Sciences of the Czech Republic, Fričova 298, CZ-251 65 Ondřejov, Czech Republic; had@sunstel.asu.cas.cz, koubsky@sunstel.asu.cas.cz

<sup>6</sup>Instituto de Astrofísica de Canarias, 38200, La Laguna, Tenerife, Spain; Departamento de Astrofísica, Universidad de La Laguna, Avda. Astrofísico Francisco Sánchez, s/n, 38071 La Laguna, Spain; ahd@ll.iac.es

<sup>7</sup>Department of Physics and Astronomy, Valparaiso University, Valparaiso, IN 46383; todd.hillwig@valpo.edu

<sup>8</sup>National Optical Astronomy Observatory, P. O. Box 26732, 950 N. Cherry Ave., Tucson, AZ 85719; howell@noao.edu

<sup>9</sup>Astronomy Department, University of Washington, Box 351580, Seattle, WA 98195-1580; hwenjin@astro.washington.edu

<sup>10</sup>Astronomical Institute Anton Pannekoek, Universiteit van Amsterdam, Kruislaan 403, 1098-SJ Amsterdam, The Netherlands; lexk@science.uva.nl

<sup>11</sup>Department of Physics, Lehigh University, 16 Memorial Drive East, Bethlehem PA 18015; mcswain@lehigh.edu

We present an examination of high resolution, ultraviolet spectroscopy from *Hubble Space Telescope* of the photospheric spectrum of the O-supergiant in the massive X-ray binary HD 226868 = Cyg X-1. We analyzed this and ground-based optical spectra to determine the effective temperature and gravity of the O9.7 Iab supergiant. Using non-local thermodynamic equilibrium (non-LTE), line blanketed, plane parallel models from the TLUSTY grid, we obtain  $T_{\text{eff}} = 28.0 \pm 2.5$  kK and  $\log g \gtrsim 3.00 \pm 0.25$ , both lower than in previous studies. The optical spectrum is best fit with models that have enriched He and N abundances. We fit the model spectral energy distribution for this temperature and gravity to the UV, optical, and IR fluxes to determine the angular size of and extinction towards the binary. The angular size then yields relations for the stellar radius and luminosity as a function of distance. By assuming that the supergiant rotates synchronously with the orbit, we can use the radius – distance relation to find mass estimates for both the supergiant and black hole as a function of the distance and the ratio of stellar to Roche radius. Fits of the orbital light curve yield an additional constraint that limits the solutions in the mass plane. Our results indicate masses of  $23_{-6}^{+8}M_{\odot}$  for the supergiant and  $11_{-3}^{+5}M_{\odot}$  for the black hole.

*Subject headings:* binaries: spectroscopic — stars: early-type — stars: individual (HD 226868, Cyg X-1) — ultraviolet: stars — X-rays: binaries

## 1. Introduction

The massive X-ray binary Cygnus X-1 = HD 226868 consists of an O9.7 Iab primary (Walborn 1973) with a black hole (BH) companion. The fundamental properties of this system have been the subject of many studies, but they continue to be controversial. For example, Shaposhnikov & Titarchuk (2007) determined a relationship between black hole mass and observed X-ray properties in the low frequency, quasi-periodic oscillation – spectral index plane to derive a BH mass of  $8.7 \pm 0.8M_{\odot}$  for Cyg X-1, a value at the low end of previous estimates (Gies & Bolton 1986a; Abubekurov et al. 2005). On the other hand, Ziółkowski (2005) used temperature – luminosity relations in conjunction with evolutionary models to calculate the mass of the bright, mass donor star. Then, with the orbital mass function from Gies et al. (2003) and the method outlined by Paczyński (1974), he estimated the mass of the BH as  $13.5 - 29M_{\odot}$ , at the high end of prior estimates.

Our goal in this paper is to determine if mass estimates from these two methods can be reconciled through a re-examination of the supergiant’s spectrum to determine the stellar temperature, mass, and radius. Shortly after the X-ray source Cyg X-1 was identified with

the star HD 226868 (Bolton 1972; Webster & Murdin 1972), Walborn (1973) classified it as a normal O9.7 Iab star. The stellar temperature of a star of this type depends critically upon the model atmosphere assumptions adopted to match the line spectrum (Martins et al. 2005). From a classical curve of growth analysis of the optical spectrum of HD 226868, Canalizo et al. (1995) estimated an effective temperature of  $T_{\text{eff}} = 32 \pm 2$  kK, and they found an overabundance of He in the photosphere. Herrero et al. (1995) also estimated the temperature of the star  $T_{\text{eff}} \approx 32$  kK based upon fits of the optical line spectrum with calculated profiles from unified model atmospheres that included a non-LTE treatment of H and He but neglected line-blanketing from transitions of heavier elements. In addition, they determined values for gravity from fits of the Balmer lines that ranged from  $\log g = 3.03$  for plane-parallel models to  $\log g = 3.21$  for spherical models that included wind effects. Their results led to mass estimates of  $17.8$  and  $10.1M_{\odot}$  for the supergiant and BH, respectively. More recently, Karitskaya et al. (2008) classified HD 226868 as an ON star with a temperature of  $T_{\text{eff}} = 30.4 \pm 0.5$  kK and gravity of  $\log g = 3.31 \pm 0.07$  using a semi-gray model atmosphere that accounts for non-LTE effects in some lines and for X-ray illumination.

Here we present an analysis of the photospheric parameters for the supergiant based upon ground-based optical spectra and high-resolution, UV spectra from the *Hubble Space Telescope* Space Telescope Imaging Spectrograph (*STIS*). These *STIS* spectra were first presented by Gies et al. (2008) and Vrtilik et al. (2008) in discussions of the orbital variations observed in the stellar wind lines. We compare the optical and UV line profiles of HD 226868 with synthetic spectra based on line blanketed, non-LTE photospheric models in order to determine the stellar temperature and gravity (§2). Since the continuum flux and spectral lines of the supergiant could be influenced by X-ray heating, we search for heating effects in the orbital UV flux variations using the low/hard state *International Ultraviolet Explorer* (*IUE*) archival spectra and the high/soft state *HST* spectra (§3). A stellar radius – distance relation can be determined from fits of the spectral energy distribution. We use the observed flux distribution and spectra of field stars in the same region of the sky to estimate the reddening and extinction in the direction of Cyg X-1 and to determine the angular size of the star (§3). Finally, we use this radius – distance relation with the method developed by Paczyński (1974) to set mass limits as a function of distance and to estimate the probable masses using constraints from the rotational line broadening and ellipsoidal light curve (§4).

## 2. Ultraviolet and Optical Line Spectrum

We need to rely on the line spectral features to estimate temperature since the UV and optical continuum falls in the long wavelength, Rayleigh-Jeans part of the flux distribution

where the shape of the continuum is insensitive to temperature. Some of the best line diagnostics for late O-supergiants are found in the optical spectrum where several ionization state line ratios and the Balmer line profiles change dramatically with temperature and gravity (Walborn & Fitzpatrick 1990; Searle et al. 2008). In this section, we use  $\chi^2_\nu$  fits of the optical and UV spectra with model spectra to estimate  $T_{\text{eff}}$  and  $\log g$ . Our data consist of high resolution UV spectra taken with the *HST*/STIS (G140M grating, resolving power  $R = 14500$ ) and two sets of optical spectra from the Kitt Peak National Observatory Coudé Feed telescope (CF; 3759 – 5086 Å,  $R = 2990$ ) and 4 m Mayall Telescope and RC spectrograph (RC; 4182 – 4942 Å,  $R = 5700$ ). Details of these observations are given in Table 1 of Gies et al. (2008). All of these flux-rectified spectra were shifted to the rest frame (using the orbital solution given by Gies et al. 2008) and co-added to increase the signal-to-noise ratio.

We compared these spectra with model spectra from the TLUSTY/SYNSPEC codes given in the grids OSTAR2002 (Lanz & Hubeny 2003) and BSTAR2006 (Lanz & Hubeny 2007). The model atmospheres are based upon a plane parallel geometry, solar abundances, line blanketed opacities, and non-LTE calculations of atomic populations for H, He, and representative atoms up to Fe. The model spectra are presented as a function of four parameters: the microturbulent velocity of gas in the line forming region,  $\xi$ , the stellar effective temperature,  $T_{\text{eff}}$ , logarithm of the gravitational acceleration in the photosphere,  $\log g$ , and the chemical abundance of the gas. The model spectra were transformed to the observed wavelength grids by wavelength integration and convolution with rotational and instrumental broadening functions. We adopted a projected rotational velocity of  $V \sin i = 98 \text{ km s}^{-1}$  (Gies & Bolton 1986a), linear limb darkening coefficients from Wade & Rucinski (1985), and Gaussian representations of instrumental broadening using the projected slit FWHM (Gies et al. 2008).

It was clear from inspection that a large microturbulence is required to match the observed and model spectra. The OSTAR2002 grid uses  $\xi = 10 \text{ km s}^{-1}$  throughout while the BSTAR2006 grid adopts  $\xi = 2 \text{ km s}^{-1}$  for the full grid and  $\xi = 10 \text{ km s}^{-1}$  for a selection of low gravity (supergiant) models. We found that the best fits were obtained in all three spectral bands with the  $\xi = 10 \text{ km s}^{-1}$  models, and this was especially true in the FUV where the observed deep spectral lines were not matched with the lower microturbulent velocity models. An atmospheric microturbulence of  $\xi = 10 \text{ km s}^{-1}$  is typical for late-O supergiants (Ryans et al. 2002), and Canalizo et al. (1995) derived an estimate of  $\xi = 10.7 \text{ km s}^{-1}$  from a curve of growth analysis of the optical N III lines in the spectrum of HD 226868.

We tested the goodness-of-fit for each of the models of interest by calculating the reduced

$\chi_\nu^2$  statistic,

$$\chi_\nu^2 = \sum_{i=0}^N \frac{[F_{obs}(\lambda_i) - F_{model}(\lambda_i)]^2}{\sigma_{err}^2(\lambda_i)(N - 1)}. \quad (1)$$

Here  $N$  is the total number of wavelength points used in the fit and  $\sigma_{err}(\lambda_i)$  is the standard deviation of the mean rectified flux (determined from the scatter at wavelength  $\lambda_i$  among the individual spectra in the co-added mean). We selectively omitted from the summation spectral regions that contained stellar wind features or interstellar lines that are not present in the model spectra. Our results are listed in Table 1 for a wide range of model spectra with a microturbulence of  $\xi = 10 \text{ km s}^{-1}$ . Column (1) indicates the spectral region fit by ‘‘HST’’ for the FUV spectrum, ‘‘CF’’ for the KPNO CF, blue spectrum, and ‘‘RC’’ for the KPNO 4 m RC, green spectrum. Column (2) gives the grid value of gravity  $\log g$ , and column (3) gives a code for the spectral model (‘‘O’’ for spectra from the OSTAR2002 grid and ‘‘B’’ and ‘‘BCN’’ for spectra from the BSTAR2006 grid). Then follow 10 columns that list the measured  $\chi_\nu^2$  for grid values of  $T_{\text{eff}}$  (at increments of 2.5 kK and 1 kK for the OSTAR2002 and BSTAR2006 grids, respectively).

The trends in Table 1 are represented in a combined contour diagram in Figure 1. Here the gray-scale contours represent the goodness-of fit for the FUV spectrum, the solid lines for the blue spectrum, and the dashed lines for the green spectrum. Since there is not an exact match between the predictions of the OSTAR2002 and BSTAR2006 grids at their boundary, Figure 1 shows contours based only on the OSTAR2002 grid for high gravity models  $\log g \geq 3.0$ , while the contours in the lower gravity region  $\log g \leq 3.0$  are based upon the BSTAR2006 grid. Note that there are no models available for high temperature, low gravity region in the lower right part of the diagram because such atmospheres approach or exceed the Eddington luminosity limit. The higher gravity, lower temperature region is empty because the BSTAR2006 grid contains only models for a lower microturbulent velocity  $\xi = 2 \text{ km s}^{-1}$  for this parameter range. Note that the  $\chi_\nu^2$  minima in Table 1 have values much larger than the expected value of unity. This is due to the inclusion of spectral regions where there is evident mismatch because of incomplete removal interstellar features, marginal differences in the continuum placement, and real differences between the observed and models even in the best fit cases. For the purposes of intercomparison in Figure 1, we have subtracted from each  $\chi_\nu^2$  set the minimum minus one value, so that the figure represents variance increases that result only from changes in the assumed temperature and gravity.

The temperature and gravity properties of the  $\chi_\nu^2$  fits shown in Figure 1 result primarily from the dependence of the spectral lines on the ionization levels in the gas. The Saha ionization equilibrium equation shows that the number ratio of atoms of one ion to the next higher ionization state is equal to the electron density times a function that decreases with increas-

ing temperature. Thus, in order to match the ionization ratios represented in the spectral line strengths, the best fits are found along a diagonal zone of increasing  $\log g$  with increasing temperature, i.e., increasing the electron density with  $\log g$  compensates for the functional drop related to temperature increase. However, there are other spectral dependences that help us determine the minimum  $\chi_\nu^2$  position along the valley in the  $(T_{\text{eff}}, \log g)$  diagram. In particular, the H Balmer line wings in the optical spectrum are sensitive to pressure broadening (linear Stark effect) and hence model gravity. The lowest contours of  $\chi_\nu^2$  in Figure 1 indicate that the best fits are found for  $T_{\text{eff}} = 26.5 - 28.5$  kK and  $\log g = 2.9 - 3.1$ . Both of these estimates are lower than found in earlier studies (Canalizo et al. 1995; Herrero et al. 1995; Karitskaya et al. 2008), but they are consistent with recent studies that demonstrate that the inclusion of line blanketing in stellar atmosphere models tends to lower the derived effective temperature (Repolust et al. 2004; Martins et al. 2005; Lefever 2007; Searle et al. 2008).

The run of  $\chi_\nu^2$  fits shown in Figure 1 are for solar abundance models, but given the reports that the spectrum of HD 226868 has strong N lines, we also explored fits with CN abundance models included in the BSTAR2006 grid for gravities of  $\log g = 2.75$  and  $3.00$ . These models assume a He to H number ratio of 0.2 (compared to 0.085 for the solar abundance models), a C abundance equal to one half the solar value, and a N abundance five times the solar abundance. These adjustments demonstrate the kind of changes that are expected when the atmosphere becomes enriched in CNO-processed gas. While the CN models do not improve the fits of the FUV spectrum, they are significantly better fits of the optical spectrum (where a number of strong He I and N III lines are present; see Fig. 2 below). When we compare the  $\chi_\nu^2$  fit of a solar model to a CN model at the same gravity in Table 1, the CN models fit better at higher temperature, especially for fits of the optical spectra. Following this trend, we estimate that the supergiant’s spectrum is fit best by the CN models with  $T_{\text{eff}} = 28 \pm 2.5$  kK and  $\log g = 3.00 \pm 0.25$  dex. Thus, we will focus on these CN models for the rest of this section.

We compare the two mean optical spectra (CF and RC) with our best fit model spectrum in Figure 2 ( $T_{\text{eff}} = 28$  kK,  $\log g = 3.00$ ) and with a marginally acceptable fit in Figure 3 ( $T_{\text{eff}} = 26$  kK,  $\log g = 2.75$ ). Also shown for comparison is the spectrum of a similar O9.7 Iab star,  $\mu$  Nor (HD 149038; from Walborn & Fitzpatrick 1990). The spectra appear in three plots: the short wavelength range from the lower resolution CF data is shown in the top panel while the bottom two panels illustrate the longer wavelength region from the higher resolution RC spectra (compare with Fig. 1 in Karitskaya et al. 2008). In general the agreement between the observed and model spectrum is satisfactory. The largest discrepancies are seen in the He II  $\lambda 4686$  and H $\beta$  lines where incipient emission from the stellar wind of the supergiant alters the profiles (Gies & Bolton 1986b; Ninkov et al. 1987a; Gies et al. 2003, 2008). The H

Balmer line emission is strongest in  $H\alpha$ , and for simple estimates of the Balmer decrement for Case B recombination (Osterbrock & Ferland 2006), we expect some measurable degree of wind emission for all the Balmer lines shown in Figures 2 and 3. We find that the H line cores do appear shallower, while the Balmer line wings agree well with the models. Searle et al. (2008) observed this effect in other supergiants and they suggest that stellar wind emission from the outer atmosphere tends to fill in the line core. On the other hand, the Balmer line wings are formed in higher density gas, deeper in the photosphere where we expect the TLUSTY/SYNSPEC results to be quite reliable. The H line wings become narrower with lower gravity, and the predicted H profiles for the lower gravity model illustrated in Figure 3 appear to be significantly narrower than the observed ones.

The He I and He II line strengths are well matched in the He enriched CN model spectra. In particular the temperature sensitive ratio of He II  $\lambda 4541$  to Si III  $\lambda 4552$  (equal for the O9.7 classification) is better reproduced by the  $T_{\text{eff}} = 28$  kK and  $\log g = 3.00$  model (Fig. 2) than the  $T_{\text{eff}} = 26$  kK and  $\log g = 2.75$  model (Fig. 3). The N III  $\lambda\lambda 4097, 4379, 4510, 4514, 4630, 4634, 4640$  lines are also reasonably well fit in the five times overabundant CN models. On the other hand, O lines like O II  $\lambda\lambda 4069, 4072, 4075, 4590, 4596$  are too strong in the model spectra, which suggests that the O abundance should be revised downwards from solar values as expected for CNO-processed gas. The other differences between the observed and model spectra are related to the presence of interstellar features (Ca II  $\lambda\lambda 3933, 3968$  in the CF spectrum; most of the deep ISM features were removed from the RC spectra).

In Figure 4 we present the averaged UV spectrum made with *HST*/STIS with the best TLUSTY/SYNSPEC model superimposed as a lighter line. Figure 4 also includes an average UV spectrum of  $\mu$  Nor, based upon 34 high resolution, archival spectra from *IUE*. Horizontal line segments indicate those regions where the lines primarily originate in the photosphere, i.e., free from P Cygni stellar wind lines and from regions where interstellar lines were removed by interpolation (Gies et al. 2008). Overall, the line features in the observed UV spectrum agree well with the model UV spectrum based upon the optimal  $T_{\text{eff}}$  and  $\log g$  parameters derived from the optical and FUV spectral fits. Note that the He II  $\lambda 1640$  feature appears in absorption as predicted, so there is no evidence of the Raman scattering emission that was observed by Kaper et al. (1990) in the massive X-ray binary 4U1700–37. There are, however, a few specific regions where the match is less satisfactory. For example, the blends surrounding Fe V  $\lambda 1422$  and Fe IV  $\lambda\lambda 1596, 1615$  appear stronger in both the spectra of HD 226868 and  $\mu$  Nor, which suggests that the models are underestimating the Fe line opacity in these wavelength regions. The S V  $\lambda 1502$  line (Howarth 1987) has a strength in the spectrum of HD 226868 that falls between that of the model and of  $\mu$  Nor. The deep feature near  $1690 \text{ \AA}$  is an instrumental flaw near the edge of the detector at one grating tilt.

There are huge variations in the stellar wind lines between the orbital conjunctions that are due to X-ray ionization of the wind (Gies et al. 2008; Vrtilik et al. 2008), and it is possible that X-ray heating might also affect some of the photospheric lines. Figure 5 compares the average UV spectra at the two conjunction phases  $\phi = 0.0$  and  $0.5$  (inferior and superior conjunction of the supergiant, respectively). With the exception of the known wind line changes, we find that the spectra are almost identical between conjunctions. Some slight differences are seen in very strong features, such as the Si III  $\lambda 1300$  complex and the Fe V line blends in the  $1600 - 1650 \text{ \AA}$  region. The deep lines appear somewhat deeper at  $\phi = 0.0$  and have slightly extended blue wings compared to those observed at  $\phi = 0.5$  (when the black hole is in the foreground). We speculate that the deeper cores and blue extensions result from line opacity that forms in the upper atmosphere where the outward wind acceleration begins. This outer part of the atmosphere in the hemisphere facing the black hole may also experience X-ray ionization (like the lower density wind) that promotes Si and Fe to higher ionization levels and reduces the line opacity of the observed transitions.

Our spectral fits are all based upon the existing OSTAR2002 and BSTAR2006 grids, and it would certainly be worthwhile to explore more specific models, for example, to derive reliable estimates of the He and N overabundances. A determination of the He abundance in particular will be important for a definitive temperature estimate. It is also important in such an analysis to consider the full effects of the stellar wind in HD 226868. Herrero et al. (1995) compared analyses of the spectrum of HD 226868 from static, plane-parallel models with unified, spherical models (that treat the photosphere and wind together), and they found their  $\log g$  estimate increased by about 0.2 dex (with no change in temperature) in the unified models. Thus, we suspect that our gravity estimate derived from the plane-parallel TLUSTY code is probably a lower limit (approximately consistent with the results of Herrero et al. 1995 and Karitskaya et al. 2005).

### 3. UV – IR Spectral Energy Distribution

We can use the derived model flux spectrum to fit the observed spectral energy distribution (SED) and reassess the interstellar extinction and the radius – distance relation. We collected the archival low dispersion *IUE* spectra and combined these fluxes with the *HST* spectra in wavelength bins spanning the FUV and NUV regions. We transformed the *UBV* magnitudes from Massey et al. (1995) into fluxes using the calibration of Colina et al. (1996), and the near-IR fluxes were determined from a calibration of the 2MASS *JHK<sub>s</sub>* magnitudes (Cohen et al. 2003; Skrutskie et al. 2006). Then we fit the observed fluxes with the optimal BSTAR2006 flux model (CN model,  $\xi = 10 \text{ km s}^{-1}$ ,  $T_{\text{eff}} = 28 \text{ kK}$ ,  $\log g = 3.0$ ) to



find the best reddening curve using the extinction law from Fitzpatrick (1999). We placed additional weight on the six optical and IR points to compensate for the larger number of UV points. Figure 6 shows the observed and best fit model fluxes for HD 226868 that we obtained with a reddening  $E(B - V) = 1.11 \pm 0.03$  mag and a ratio of total to selective extinction  $R_V = 3.02 \pm 0.03$ . These values agree well with the previous reddening estimates that are collected in Table 2.

For comparison we examined the colors and reddening of six field stars within 10 arcminutes of HD 226868 in the sky. These stars were observed with the KPNO 4 m telescope and RC spectrograph using the same blue region arrangement selected for our observations of HD 226868 (Gies et al. 2008). We made spectral classification of the stars, and then we used the observed  $UBV$  colors from Massey et al. (1995) and the intrinsic color and absolute magnitude for the classification (Gray 1992) to estimate reddening and distances to these stars. Our results are collected in Table 3 with the reddening estimate from above listed for HD 226868. Bregman et al. (1973) estimated the distance of HD 226868 as  $d \approx 2.5$  kpc, and set a lower limit of 1 kpc based upon the colors of other nearby field stars. We find that there are two stars at distances just under 1 kpc that have a similar reddening to that of HD 226868, which is consistent with a distance to HD 226868 of  $d \gtrsim 1.0$  kpc.

The normalization of the fit to the SED yields the star’s limb-darkened angular diameter,  $\theta = 96 \pm 6 \mu\text{as}$ . Then we can calculate the luminosity and radius of the star as a function of distance  $d$  (in kpc) to HD 226868,

$$\frac{L_1}{L_\odot} = (5.9 \pm 2.1) \times 10^4 d^2, \quad (2)$$

$$\frac{R_1}{R_\odot} = (10.3 \pm 0.7)d. \quad (3)$$

It is important to check that these SED results are not affected by long term or orbital flux variability, so we examined the archival *IUE* low dispersion spectra (Gies et al. 2008) and the *HST* spectra to determine the amplitude of any flux variations in the UV. We calculated the average continuum flux over three wavelength spans (1252 – 1380 Å, 1410 – 1350 Å, and 1565 – 1685 Å) that excluded the main wind features. We then converted the UV fluxes to differential magnitudes  $\Delta m$ . We found no significant differences between fluxes from times corresponding to the X-ray low/hard state (*IUE*) and high/soft state (*IUE* and *HST*; see Gies et al. 2008 for X-ray state information), nor were there any long term variations over the 25 year time span between the *IUE* and *HST* observations. On the other hand, we do find marginal evidence of the orbital flux variations related to the tidal distortion of the supergiant. We plot in Figure 7 the mean orbital flux variations of the three wavelength intervals for both *IUE* and *HST* spectra that are averaged into eight bins of orbital phase. For

comparison we also include the  $V$ -band ellipsoidal light curve from Khaliullin & Khaliullina (1981). The UV and  $V$ -band light curves appear to have similar amplitudes, consistent with past estimates (Treves et al. 1980; van Loon et al. 2001). Note that the minima have approximately equal depths (consistent with the optical results; Balog et al. 1981), which suggests that there is little if any deep heating by X-rays of the hemisphere of the supergiant facing the black hole. Since the amplitude of the light curve is small and the average UV fluxes plotted in the SED in Figure 6 cover the full orbit, the ellipsoidal variations have a minimal impact on the quantities derived from the SED.

Finally, we need to consider if the SED has a non-stellar flux contribution from the accretion disk around the black hole or from other circumstellar gas. Bruevich et al. (1978) estimated that the disk contributes about 2% of the optical flux, and there are reports of small optical variations with superorbital periods that may correspond to the precession of the accretion disk (Kemp et al. 1987; Brocksopp et al. 1999; Szostek & Zdziarski 2007; Poutanen et al. 2008). Furthermore, Dolan (2001) observed rapid UV variations that he argued originate in dying pulse trains of infalling material passing the event horizon of the BH. Miller et al. (2002) developed a multi-color disk SED to model the X-ray continuum of Cyg X-1, and Dr. Miller kindly sent us the model fluxes extrapolated into the UV and optical. These are also plotted in Figure 6 after accounting for interstellar extinction. Both the photospheric and disk SEDs correspond to the Rayleigh-Jeans tail of a hot continuum, and the model predicts that the disk contributes approximately 0.01% of the total flux in the UV to IR range. This small fraction is consistent with our successful fitting of the UV and optical line features that would otherwise appear shallower by flux dilution if the disk was a significant flux contributor. Thus, our SED fitting is probably unaffected by any non-stellar flux source.

#### 4. Mass of the Supergiant

In this section we will explore the mass consequences of our relations for radius and luminosity as a function of distance. Paczyński (1974) derived model-independent, minimum mass estimates for both components as a function of distance based on the lack of X-ray eclipses (setting a maximum orbital inclination) and the assumption that HD 226868 is not larger than its Roche lobe (setting a lower limit on the ratio of the supergiant to black hole mass,  $M_1/M_2$ ). We repeated his analysis using our revised radius – distance relationship (eq. [3]), stellar effective temperature  $T_{\text{eff}} = 28$  kK, and current values for the mass function  $f(m) = 0.251 \pm 0.007 M_{\odot}$  and period  $P = 5.599829$  days (Gies et al. 2003). The resulting minimum masses are presented in columns 7 and 10 of Table 4 as a function of distance  $d$ .

We can make further progress by assuming the supergiant has attained synchronous rotation with the orbit since the stellar radius is probably comparable in size to the Roche radius (Gies & Bolton 1986b). We take the ratio  $\Omega$  of the star’s spin angular velocity to orbital angular velocity to be 1. Then the projected rotational velocity  $V \sin i$  is related to the inclination  $i$  by

$$V \sin i = \frac{2\pi}{P} R_1 \sin i \quad (4)$$

where  $P$  is the orbital period. The projected rotational velocity, after correction for macro-turbulent broadening, is estimated to be  $V \sin i = 95 \pm 6 \text{ km s}^{-1}$  (Gies & Bolton 1986a; Ninkov et al. 1987b; Herrero et al. 1995). Inserting equation (3) for  $R_1$  we obtain an inclination estimate in terms of distance  $d$  (kpc) of

$$i = \arcsin((1.02 \pm 0.09)d). \quad (5)$$

These inclination estimates are given in column 2 of Table 4. Note that this argument suggests a lower limit to the distance of  $\approx 1.0$  kpc, similar to that found by reddening considerations.

Gies & Bolton (1986a) showed that the mass ratio can be estimated from the ratio of the projected rotational velocity to the orbital semiamplitude of the supergiant,

$$\frac{V \sin i}{K} = \rho(Q + 1)\Phi(Q) \quad (6)$$

where  $\rho$  is the fill-out factor, i.e., the ratio of volume equivalent radii of the star and Roche lobe,  $Q = M_1/M_2$  is the mass ratio,  $\Phi$  is the ratio of the Roche lobe radius to the semimajor axis (Eggleton 1983), and synchronous rotation is assumed. Thus, given the observed values of  $V \sin i$  and  $K$  and an assumed value of  $\rho$ , we can find the mass ratio and, with the inclination, the masses of each star. These masses are listed in columns 8, 9, 11 and 12 of Table 4 under headings that give the fill-out factor in parentheses. The run of masses is also shown in Figure 8 that illustrates the mass solutions as a function of distance and fill-out factor. Loci of constant  $\rho$  are denoted by dotted lines (increasing right to left from  $\rho = 0.85$  to 1.0) while loci of constant distance (and inclination angle) are shown by dashed lines. The derived gravity values from these masses of  $\log g \approx 3.3$  reinforces the idea that our spectral estimate of  $\log g = 3.0$  is a lower limit (see §2).

We assumed synchronous rotation in the relations above because both observations and theory indicate that the orbital synchronization time scale in close binaries is shorter than the circularization time scale (Claret et al. 1995), and since the orbit is circular, it follows that the star must rotate at close to the synchronous rate. However, it is straight forward to see how the solutions will change if the synchronism parameter  $\Omega$  differs from unity. In

equation (5) the distance  $d$  can be replaced by the product  $\Omega d$ , while in equation (6) the fill-out parameter  $\rho$  can be replaced by  $\Omega\rho$ . If, for example,  $\Omega = 0.95$ , then the mass solutions can be obtained from Table 4 and Figure 8 by selecting a distance of  $0.95d$  and a fill-out ratio of  $0.95\rho$ .

The other important constraint comes from the ellipsoidal light curve. The tidal distortion of the star results in a double-wave variation (Fig. 7) whose amplitude depends on the inclination (maximal at  $i = 90^\circ$ ) and degree of tidal distortion (maximal for fill-out  $\rho = 1.0$ ). In order to determine which parts of mass plane are consistent with the observed variation, we constructed model  $V$ -band light curves using the GENSYN code (Mochnacki & Doughty 1972; Gies & Bolton 1986a) for the four values of fill-out factor illustrated in Figure 8. There is a unique solution for the best fit of the light curve along each line of constant fill-out factor, since the light curve amplitude monotonically decreases with decreasing inclination (increasing distance). The solid line in Figure 8 connects these best fit solutions (indicated by plus sign symbols). These light curve solutions differ slightly from those presented by Gies & Bolton (1986a) because we chose to fit the light curve from Khaliullin & Khaliullina (1981) instead of that from Kemp et al. (1983), and the differences in the solutions reflect the uncertainties in the observed light curve.

There are several other constraints from hints about the mass transfer process, luminosity, and distance that can provide additional limits on the acceptable mass ranges. Both Gies & Bolton (1986b) and Ninkov et al. (1987a) presented arguments that the unusual He II  $\lambda 4686$  emission in the spectrum of HD 226868 originates in a tidal stream or focused wind from the supergiant towards the black hole. Furthermore, Gies & Bolton (1986b) made radiative transfer calculations of the focused wind emission profiles for models of the asymmetric wind from Friend & Castor (1982), and they determined that the fill-out factor must exceed  $\rho = 0.90$  in order to increase sufficiently the wind density between the stars to account for the observed strength of the He II  $\lambda 4686$  emission. Thus, the presence of a focused wind implies that the fill-out factor falls in the range  $\rho = 0.9 - 1.0$ .

Paczyński (1974) and Ziółkowski (2005) argue that massive stars evolve at near constant luminosity, and, therefore, the best solutions will obey the observed mass – luminosity relation. Table 4 lists the derived luminosity  $\log L_1$  (column 4) as a function of distance (eq. [2]) plus the predicted luminosities for the mass solutions determined for the  $\rho = 0.9$  and  $1.0$  cases,  $\log L_1^*(0.9)$  and  $\log L_1^*(1.0)$ , respectively (columns 5 and 6). These predictions are based upon the mass – luminosity relations for  $T_{\text{eff}} = 28$  kK stars from the model evolutionary sequences made by Schaller et al. (1992). We find that the observed and predicted luminosities match over the distance range of  $d = 1.7$  ( $\rho = 0.9$ ) to  $2.0$  kpc ( $\rho = 1.0$ ), closer than the range advocated by Ziółkowski (2005) who adopted a higher temperature and hence

higher luminosity. Note that some stars in mass transfer binaries appear overluminous for their mass, so these distances should probably be considered as upper limits.

Several authors have suggested that the position and proper motion of HD 226868 indicates that it is a member of the Cyg OB3 association (Mirabel & Rodrigues 2003) that has a distance of 1.6-2.5 kpc (Uyaniker et al. 2001). However, a radio parallax study by Lestrade et al. (1999) indicates a smaller (but possibly consistent) distance of  $1.4_{-0.4}^{+0.9}$  kpc for Cyg X-1. Our fits of the ellipsoidal light curve suggest that the maximum allowable distance is  $d \approx 2.0$  kpc (for  $\rho = 1.0$ ) The interstellar reddening indicates a distance of at least 1.0 kpc (§3), which is probably consistent with the strength of interstellar Ca II lines. Megier et al. (2005) present a method for determining the distance to O supergiants using the equivalent width  $W_\lambda$  of the Ca II  $\lambda 3933$  feature. Using their calibration with the value of  $W_\lambda = 400 \pm 10$  mÅ from Gies & Bolton (1986a) yields a distance  $d = 1.2$  kpc. Since the reddening of HD 226868 is approximately the same as that for the much more distant Cepheid, V547 Cyg (Bregman et al. 1973), the ISM must have a relatively low density beyond  $\approx 1$  kpc along this line of sight through the Galaxy, so we suspect that the distance derived from the interstellar Ca II line is probably a lower limit.

All of these constraints are consistent with the mass solutions for a fill-out factor range of  $\rho = 0.9 - 1.0$ , and the corresponding mass ranges are listed in Table 5. We also list mass estimates from earlier investigations. Our downward revision of the effective temperature results in lower luminosity estimates than adopted by Ziółkowski (2005), and consequently, our mass estimates (based upon the light curve) are significantly lower than his mass estimates (based upon the mass – luminosity relation from models). In fact, the lower limit for the black hole mass now overlaps comfortably with the mass determined by Shaposhnikov & Titarchuk (2007) using the correlation between the X-ray quasi-periodic oscillation frequency and spectral index, so the apparent discrepancy in black hole mass estimates from X-ray and optical data is now resolved. If the X-ray derived mass is accurate, then the mass solution for fill-out factor  $\rho = 0.91$  is preferred ( $M_1 = 19M_\odot$  and the distance is  $d = 1.6$  kpc).

Our analysis of the first high resolution UV spectra of HD 226868 and of the complementary optical spectra shows that the photospheric line spectrum can be matched by adopting an atmosphere mixed with CNO-processed gas with an effective temperature  $T_{\text{eff}} = 28.0 \pm 2.5$  kK and  $\log g \gtrsim 3.0 \pm 0.25$ . Assuming synchronous rotation ( $\Omega = 1$ ) and using the fill-out factor range from above, the mass of the supergiant ranges from  $M_1 = 17 - 31M_\odot$  and the black hole mass ranges from  $M_2 = 8 - 16M_\odot$ . This corresponds to an inclination of  $i = 31^\circ - 43^\circ$  and a distance of  $d = 1.5 - 2.0$  kpc. Better estimates of the masses may be possible in the future. For example, both the *GAIA* (Jordan 2008) and *SIM Lite* (Unwin et al. 2008) space astrometry missions will provide an accurate parallax

and distance. Furthermore, pointed observations with SIM Lite will measure the astrometric motion of the supergiant around the system center of mass, yielding independent estimates of both the orbital inclination and distance (by equating the astrometric and radial velocity semi-major axes; Tomsick et al. 2009). Finally, future high dispersion X-ray spectroscopy with the *International X-ray Observatory*<sup>12</sup> will measure the orbital motion of the black hole through the orbital Doppler shifts of accretion disk flux in the Fe K $\alpha$  line (Miller 2007). By comparing the optical and X-ray orbital velocity curves, we will have a secure mass ratio that, together with the distance estimate, will lead to unique and accurate mass determinations of the supergiant and black hole.

We thank the staffs of the Kitt Peak National Observatory and the Space Telescope Science Institute (STScI) for their support in obtaining these observations. We are also grateful to Thierry Lanz and Ivan Hubeny for information about their model atmosphere grid and to Jon Miller for providing us with details about his accretion disk model. Support for *HST* proposal number GO-9840 was provided by NASA through a grant from the Space Telescope Science Institute, which is operated by the Association of Universities for Research in Astronomy, Incorporated, under NASA contract NAS5-26555. The *IUE* data presented in this paper were obtained from the Multimission Archive at the Space Telescope Science Institute (MAST). Support for MAST for non-HST data is provided by the NASA Office of Space Science via grant NAG5-7584 and by other grants and contracts. This publication makes use of data products from the Two Micron All Sky Survey, which is a joint project of the University of Massachusetts and the Infrared Processing and Analysis Center/California Institute of Technology, funded by the National Aeronautics and Space Administration and the National Science Foundation. Bolton’s research is partially supported by a Natural Sciences and Engineering Research Council of Canada (NSERC) Discovery Grant. Hadrava’s research is funded under grant projects GAČR 202/06/0041 and LC06014. Herrero thanks the Spanish MEC for support under project AY 2007-67456-C02-01. This work was also supported by the National Science Foundation under grants AST-0205297, AST-0506573, and AST-0606861. Institutional support has been provided from the GSU College of Arts and Sciences and from the Research Program Enhancement fund of the Board of Regents of the University System of Georgia, administered through the GSU Office of the Vice President for Research. We are grateful for all this support.

---

<sup>12</sup><http://ixo.gsfc.nasa.gov/index.html>

## REFERENCES

- Abubekerov, M. K., Antokhina, É. A., & Cherepashchuk, A. M. 2005, *Astronomy Reports*, 49, 801
- Balog, N. I., Goncharskij, A. V., & Cherepashchuk, A. M. 1981, *Soviet Astronomy Letters*, 7, 336
- Bolton, C. T. 1972, *Nature*, 240, 124
- Bregman, J., Butler, D., Kemper, E., Koski, A., Kraft, R. P., & Stone, R. P. P. 1973, *ApJ*, 185, L117
- Brocksopp, C., Fender, R. P., Larionov, V., Lyuty, V. M., Tarasov, A. E., Pooley, G. G., Paciesas, W. S., & Roche, P. 1999, *MNRAS*, 309, 1063
- Bruevich, V. V., Kiliachkov, N. N., Syunyaev, R. A., & Shevchenko, V. S. 1978, *Soviet Astronomy Letters*, 4, 292
- Canalizo, G., Koenigsberger, G., Peña, D., & Ruiz, E. 1995, *Revista Mexicana de Astronomía y Astrofísica*, 31, 63
- Claret, A., Giménez, A., & Cunha, N. C. S. 1995, *A&A*, 299, 724
- Cohen, M., Wheaton, W. A., & Megeath, S. T. 2003, *AJ*, 126, 1090
- Colina, L., Bohlin, R., & Castelli, F. 1996, *HST Instrument Science Report CAL/SCS-008* (Baltimore: STScI)
- Dolan, J. F. 2001, *PASP*, 113, 974
- Eggleton, P. P. 1983, *ApJ*, 268, 368
- Fitzpatrick, E. L. 1999, *PASP*, 111, 63
- Friend, D. B., & Castor, J. I. 1982, *ApJ*, 261, 293
- Gies, D. R., & Bolton, C. T. 1986a, *ApJ*, 304, 371
- . 1986b, *ApJ*, 304, 389
- Gies, D. R. et al. 2008, *ApJ*, 678, 1237
- . 2003, *ApJ*, 583, 424

- Gray, D. F. 1992, *The Observation and Analysis of Stellar Photospheres*, 2nd edn. (Cambridge: Cambridge Univ. Press)
- Herrero, A., Kudritzki, R. P., Gabler, R., Vilchez, J. M., & Gabler, A. 1995, *A&A*, 297, 556
- Howarth, I. D. 1987, *MNRAS*, 226, 249
- Jordan, S. 2008, *Astronomische Nachrichten*, 329, 875
- Kaper, L., Hammerschlag-Hensberge, G., & Takens, R. J. 1990, *Nature*, 347, 652
- Karitskaya, E. A. et al. 2005, *Astronomical and Astrophysical Transactions*, 24, 383
- Karitskaya, E. A., Bochkarev, N. G., Bondar', A. V., Galazutdinov, G. A., Lee, B.-C., Musaev, F. A., Sapar, A. A., & Shimanskii, V. V. 2008, *Astronomy Reports*, 52, 362
- Kemp, J. C. et al. 1983, *ApJ*, 271, L65
- Kemp, J. C., Karitskaya, E. A., Kumsiashvili, M. I., Lyutyi, V. M., Khruzina, T. S., & Cherepashchuk, A. M. 1987, *Soviet Astronomy*, 31, 170
- Khaliullin, K. F., & Khaliullina, A. I. 1981, *Soviet Astronomy*, 25, 593
- Lanz, T., & Hubeny, I. 2003, *ApJS*, 146, 417
- . 2007, *ApJS*, 169, 83
- Lefever, K. 2007, Ph.D. Thesis (Katholieke Universiteit Leuven)
- Lestrade, J.-F., Preston, R. A., Jones, D. L., Phillips, R. B., Rogers, A. E. E., Titus, M. A., Rioja, M. J., & Gabuzda, D. C. 1999, *A&A*, 344, 1014
- Martins, F., Schaerer, D., & Hillier, D. J. 2005, *A&A*, 436, 1049
- Massey, P., Johnson, K. E., & Degioia-Eastwood, K. 1995, *ApJ*, 454, 151
- Megier, A., Strobel, A., Bondar, A., Musaev, F. A., Han, I., Krelowski, J., & Galazutdinov, G. A. 2005, *ApJ*, 634, 451
- Miller, J. M. 2007, *ARA&A*, 45, 441
- Miller, J. M. et al. 2002, *ApJ*, 578, 348
- Mirabel, I. F., & Rodrigues, I. 2003, *Science*, 300, 1119
- Mochnacki, S. W., & Doughty, N. A. 1972, *MNRAS*, 156, 51



- Ninkov, Z., Walker, G. A. H., & Yang, S. 1987a, *ApJ*, 321, 438
- . 1987b, *ApJ*, 321, 425
- Osterbrock, D. E., & Ferland, G. J. 2006, *Astrophysics of Gaseous Nebulae and Active Galactic Nuclei*, 2nd edn. (Sausalito, CA: University Science Books)
- Paczynski, B. 1974, *A&A*, 34, 161
- Poutanen, J., Zdziarski, A. A., & Ibragimov, A. 2008, *MNRAS*, 389, 1427
- Repolust, T., Puls, J., & Herrero, A. 2004, *A&A*, 415, 349
- Ryans, R. S. I., Dufton, P. L., Rolleston, W. R. J., Lennon, D. J., Keenan, F. P., Smoker, J. V., & Lambert, D. L. 2002, *MNRAS*, 336, 577
- Savage, B. D., Massa, D., Meade, M., & Wesselius, P. R. 1985, *ApJS*, 59, 397
- Schaller, G., Schaerer, D., Meynet, G., & Maeder, A. 1992, *A&AS*, 96, 269
- Searle, S. C., Prinja, R. K., Massa, D., & Ryans, R. 2008, *A&A*, 481, 777
- Shaposhnikov, N., & Titarchuk, L. 2007, *ApJ*, 663, 445
- Skrutskie, M. F. et al. 2006, *AJ*, 131, 1163
- Szostek, A., & Zdziarski, A. A. 2007, *MNRAS*, 375, 793
- Tomsick, J., Shaklan, S., & Pan, X. 2009, in *SIMLite Astrometric Observatory*, ed. J. Davidson, S. Edberg, R. Danner, B. Nemati, & S. Unwin (Pasadena: NASA JPL 400-1360), 97
- Treves, A. et al. 1980, *ApJ*, 242, 1114
- Unwin, S. C. et al. 2008, *PASP*, 120, 38
- Uyaniker, B., Fürst, E., Reich, W., Aschenbach, B., & Wielebinski, R. 2001, *A&A*, 371, 675
- van Loon, J. T., Kaper, L., & Hammerschlag-Hensberge, G. 2001, *A&A*, 375, 498
- Vrtilek, S. D., Boroson, B. S., Hunacek, A., Gies, D., & Bolton, C. T. 2008, *ApJ*, 678, 1248
- Wade, R. A., & Rucinski, S. M. 1985, *A&AS*, 60, 471
- Walborn, N. R. 1973, *ApJ*, 179, L123

Walborn, N. R., & Fitzpatrick, E. L. 1990, *PASP*, 102, 379

Webster, B. L., & Murdin, P. 1972, *Nature*, 235, 37

Wegner, W. 2002, *Baltic Astronomy*, 11, 1

Wu, C.-C., Eaton, J. A., Holm, A. V., Milgrom, M., & Hammerschlag-Hensberge, G. 1982, *PASP*, 94, 149

Ziółkowski, J. 2005, *MNRAS*, 358, 851

Table 1.  $\chi^2_\nu$  for Spectral Fits with Models

Spectrum	log $g$	Model	$T_{\text{eff}}$ (kK)									
			Source	(cm s $^{-2}$ )	Code	24.0	25.0	26.0	27.0	27.5	28.0	29.0
HST	4.00	O	...	...	...	...	35.6	...	...	24.4	24.1	29.3
HST	3.75	O	...	...	...	...	30.7	...	...	23.0	24.7	33.4
HST	3.50	O	...	...	...	...	26.0	...	...	22.6	27.0	42.8
HST	3.25	O	...	...	...	...	22.8	...	...	23.8	36.2	77.5
HST	3.00	O	...	...	...	...	23.0	...	...	32.8	...	...
HST	3.00	B	39.5	29.1	24.1	23.0	...	24.1	27.3	34.8	...	...
HST	3.00	BCN	42.5	31.7	25.5	23.6	...	23.9	25.9	31.6	...	...
HST	2.75	B	28.5	25.9	27.0	31.7	...	...	...	...	...	...
HST	2.75	BCN	31.6	26.5	26.2	28.5	...	...	...	...	...	...
CF	4.00	O	...	...	...	...	114.5	...	...	72.2	53.0	43.7
CF	3.75	O	...	...	...	...	87.8	...	...	55.8	36.7	43.5
CF	3.50	O	...	...	...	...	59.3	...	...	29.6	30.7	53.9
CF	3.25	O	...	...	...	...	32.5	...	...	21.2	47.7	85.5
CF	3.00	O	...	...	...	...	19.6	...	...	51.0	...	...
CF	3.00	B	51.0	36.9	24.4	16.7	...	16.2	27.9	50.0	...	...
CF	3.00	BCN	59.2	44.8	30.6	19.4	...	12.9	13.5	31.4	...	...
CF	2.75	B	22.4	17.3	23.7	51.9	...	...	...	...	...	...
CF	2.75	BCN	28.7	17.2	12.5	20.2	...	...	...	...	...	...
RC	4.00	O	...	...	...	...	85.9	...	...	42.0	25.1	42.7
RC	3.75	O	...	...	...	...	68.3	...	...	31.9	22.7	61.3
RC	3.50	O	...	...	...	...	50.0	...	...	20.8	38.9	92.5
RC	3.25	O	...	...	...	...	33.6	...	...	24.5	85.5	143.4
RC	3.00	O	...	...	...	...	25.2	...	...	90.5	...	...
RC	3.00	B	88.1	61.3	35.9	19.8	...	19.6	51.5	106.6	...	...
RC	3.00	BCN	112.9	83.8	53.7	29.7	...	15.6	17.9	62.6	...	...
RC	2.75	B	47.7	25.1	29.4	95.7	...	...	...	...	...	...
RC	2.75	BCN	69.2	36.3	17.1	26.3	...	...	...	...	...	...

Table 2. Interstellar Reddening Estimates

Source	$E(B - V)$	$R_V$
Bregman et al. (1973)	1.12 (5)	3.0
Treves et al. (1980)	1.06	3.0
Wu et al. (1982)	0.95 (7)	3.1
Savage et al. (1985)	1.080 (25)	3.1
Wegner (2002)	1.03	3.32
This Paper	1.11 (3)	3.02 (3)

Note. — Numbers in parentheses give the error in the last digit quoted.

Table 3. Interstellar Reddening for HD 226868 and Nearby Stars

R.A. (2000) (hh mm ss.ss)	Dec. (2000) (dd mm ss.s)	Spectral Classification	$m_V$ (mag)	$m_B$ (mag)	$E(B - V)$ (mag)	$d$ (kpc)
19 58 21.68	+35 12 05.8	O9.7 Iab	8.81	9.64	1.11	...
19 58 23.44	+35 14 32.2	A3 V	15.15	16.46	1.26	0.98
19 58 29.31	+35 09 27.5	G0 V	15.11	16.35	0.66	0.54
19 58 04.44	+35 11 48.3	G2 V	15.06	15.97	0.28	0.82
19 58 02.06	+35 14 00.0	F2 V	15.37	16.74	1.02	0.73
19 58 57.44	+35 05 31.7	G2 V	15.42	16.43	0.38	0.84
19 58 44.45	+35 08 09.8	F5 V	15.76	16.87	0.68	1.07

Table 4. Mass and Luminosity versus Distance for HD 226868

$d$ (kpc)	$i$ ( $^\circ$ )	$R_1$ ( $R_\odot$ )	$\log L_1$ ( $L_\odot$ )	$\log L_1^*(0.9)$ ( $L_\odot$ )	$\log L_1^*(1.0)$ ( $L_\odot$ )	$M_1^{min}$ ( $M_\odot$ )	$M_1^{sync}(0.9)$ ( $M_\odot$ )	$M_1^{sync}(1.0)$ ( $M_\odot$ )	$M_2^{min}$ ( $M_\odot$ )	$M_2^{sync}(0.9)$ ( $M_\odot$ )	$M_2^{sync}(1.0)$ ( $M_\odot$ )
1.1	67.5	11.4	4.85	3.06	2.77	5.0	6.6	5.0	2.7	3.1	2.6
1.2	57.9	12.4	4.93	3.41	3.04	6.4	8.6	6.5	3.1	4.0	3.4
1.3	51.4	13.4	5.00	3.83	3.35	7.9	10.9	8.2	3.5	5.0	4.3
1.4	46.5	14.5	5.06	4.31	3.71	9.6	13.7	10.3	4.0	6.3	5.4
1.5	42.6	15.5	5.12	4.70	4.13	11.6	16.8	12.7	4.5	7.7	6.6
1.6	39.4	16.5	5.18	4.99	4.57	13.8	20.4	15.4	5.0	9.4	8.0
1.7	36.7	17.6	5.23	5.21	4.85	16.3	24.5	18.4	5.5	11.3	9.6
1.8	34.4	18.6	5.28	5.37	5.08	19.0	29.0	21.9	6.1	13.4	11.4
1.9	32.3	19.6	5.33	5.54	5.26	21.9	34.1	25.7	6.6	15.7	13.4
2.0	30.5	20.7	5.37	5.68	5.40	25.2	39.8	30.0	7.2	18.4	15.6
2.1	28.9	21.7	5.41	5.80	5.56	28.7	46.1	34.7	7.9	21.3	18.1
2.2	27.5	22.7	5.45	5.92	5.69	32.5	53.0	39.9	8.5	24.4	20.8
2.3	26.2	23.8	5.49	6.05	5.79	36.7	60.6	45.6	9.2	27.9	23.8
2.4	25.0	24.8	5.53	6.17	5.90	41.1	68.8	51.9	9.9	31.7	27.0
2.5	24.0	25.9	5.57	6.27	6.02	45.9	77.8	58.6	10.6	35.9	30.5

Table 5. Mass Estimates

Source	$M_1$ ( $M_\odot$ )	$M_2$ ( $M_\odot$ )
Balog et al. (1981)	20 – 27	7 – 12
Gies & Bolton (1986a)	23 – 38	10 – 20
Ninkov et al. (1987b)	20	10
Herrero et al. (1995)	17.8	10.1
Abubekerov et al. (2005)	22	8.2 – 12.8
Ziółkowski (2005)	30 – 50	13.5 – 29
Shaposhnikov & Titarchuk (2007)	...	7.9 – 9.5
This paper	17 – 31	8 – 16

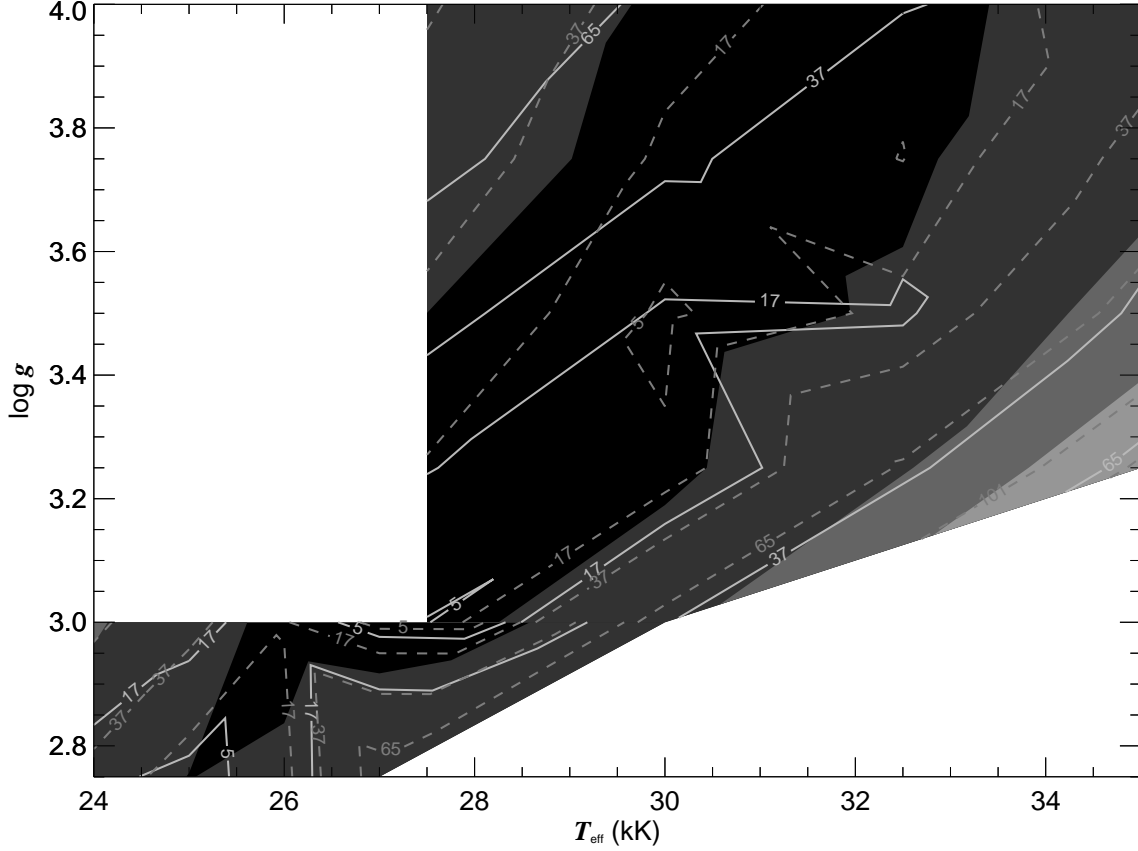


Fig. 1.— The variation within the  $(T_{\text{eff}}, \log g)$  plane of the net reduced  $\chi_{\nu}^2$  statistic that measures the goodness of fit between the solar abundance models and the observed spectrum of HD 226868. The contours show the value of  $\chi_{\nu}^2$  above the best fit minimum (arbitrarily set to one), and they nominally represent the intervals of  $2\sigma$ ,  $4\sigma$ , ... $10\sigma$  where  $\sigma$  is the error in the parameter estimate. The contours for the FUV, KPNO CF, and KPNO 4 m spectral fits are shown as different gray-shaded regions, solid lines, and dashed lines, respectively. The contours for  $\log g \leq 3.0$  are for fits with the BSTAR2006 models, while those for  $\log g \geq 3.0$  are for fits with the OSTAR2002 models.

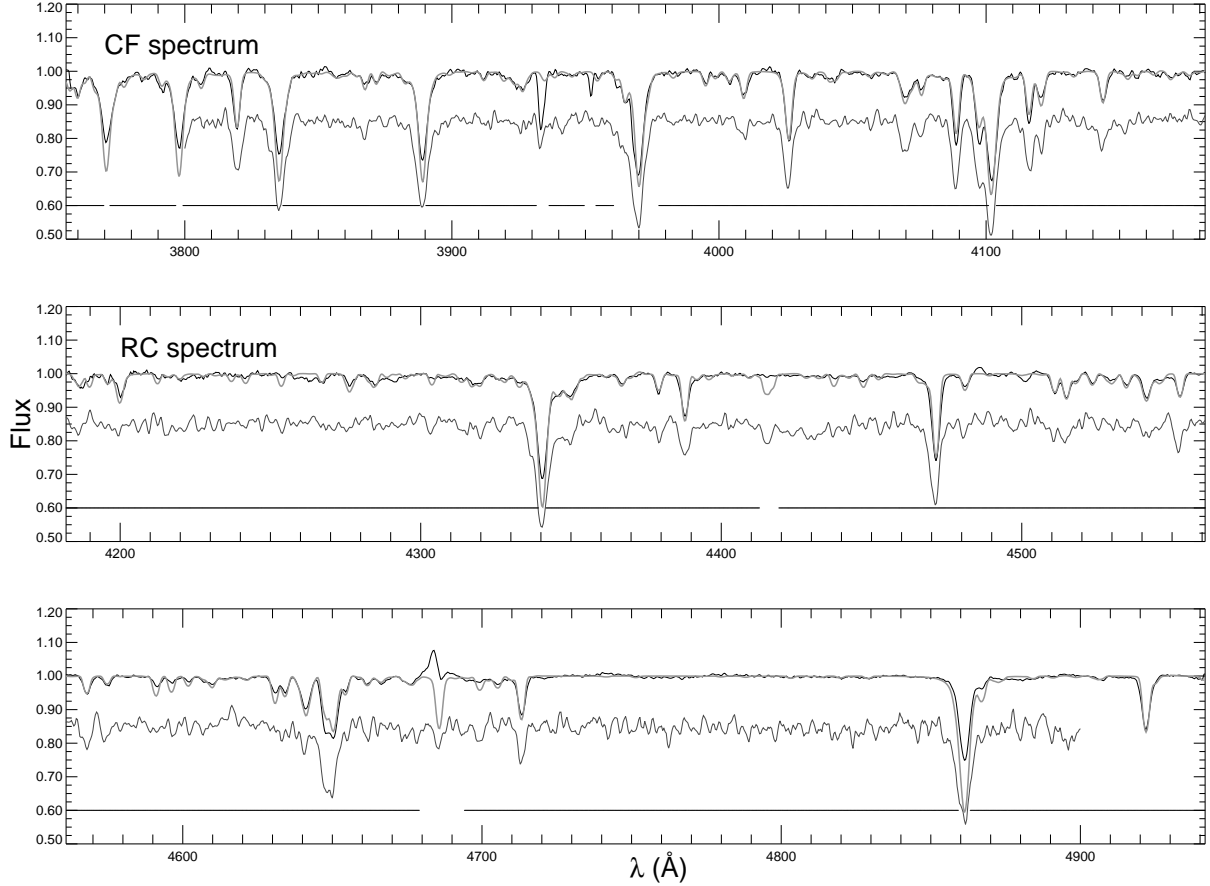


Fig. 2.— Rectified optical spectra (*dark line*) together with a  $T_{\text{eff}} = 28$  kK and  $\log g = 3.0$  TLUSTY CN model (*light line*). The top panel shows the mean spectrum obtained with the KPNO Coudé Feed telescope while the bottom two panels show the mean spectrum obtained with the KPNO 4-m telescope. The spectrum of the O9.7 Iab star  $\mu$  Nor is offset by 0.15 from the model and HD 226868 spectra for comparison. The horizontal lines below the spectra indicate the wavelength regions included in the  $\chi^2_\nu$  calculation. The He II  $\lambda 4686$  emission line originates in the focused wind from the star.



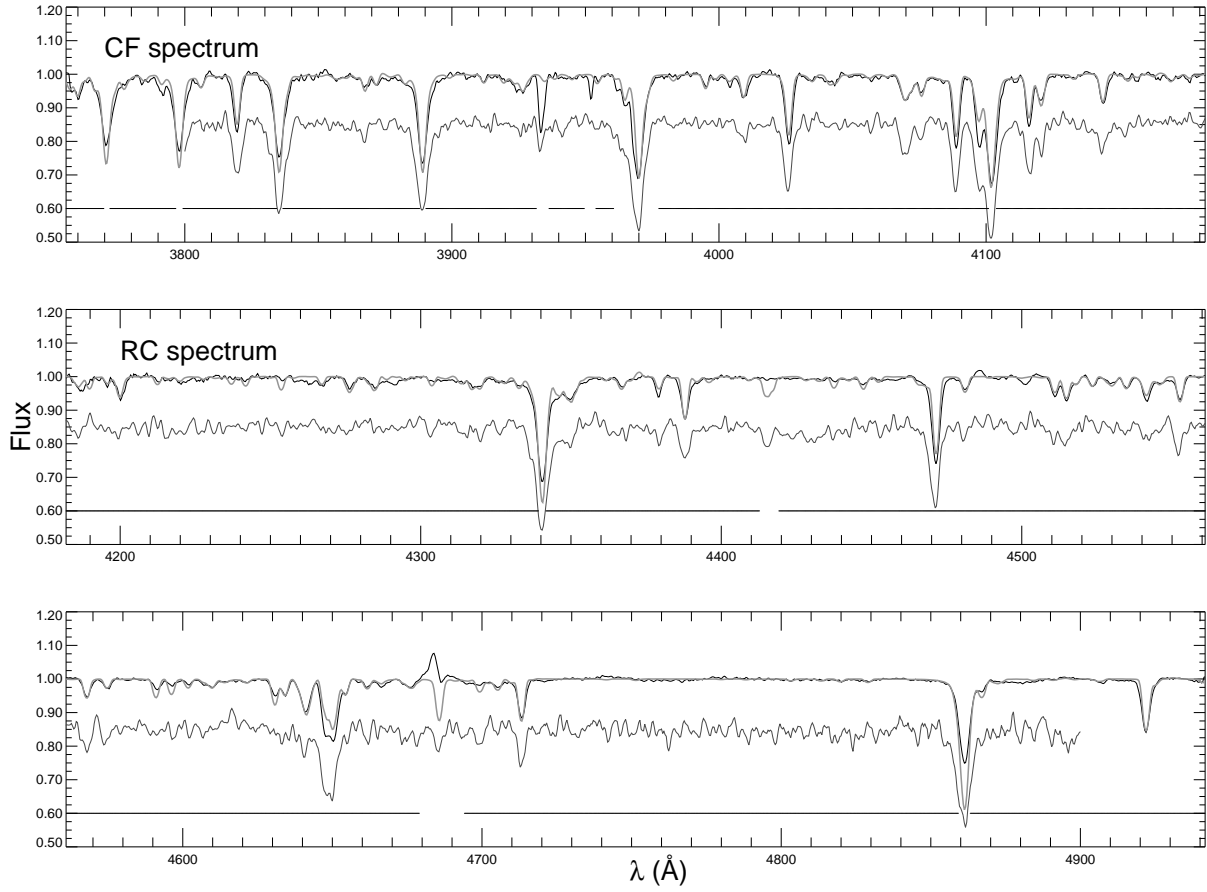


Fig. 3.— Optical spectra (*dark line*) together with a  $T_{\text{eff}} = 26$  kK and  $\log g = 2.75$  TLUSTY CN model (*light line*) in the same format as Fig. 2.

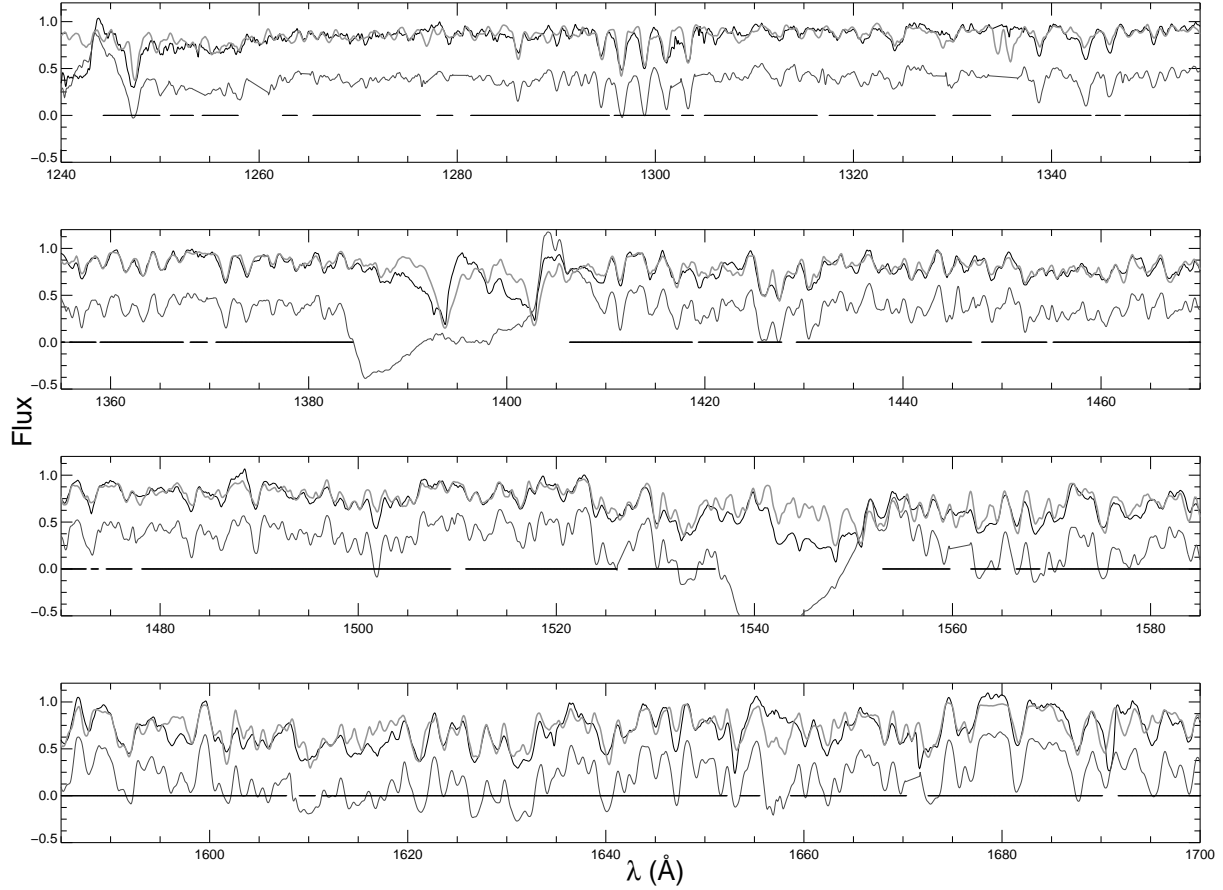


Fig. 4.— Observed UV spectrum (*dark line*) plus a TLUSTY CN model spectrum for  $T_{\text{eff}} = 28$  kK and  $\log g = 3.0$  (*light line*). The spectrum of the O9.7 Iab star  $\mu$  Nor is offset by 0.6 from the model and HD 226868 spectra for comparison. The horizontal lines below the spectra indicate regions included in the  $\chi^2_\nu$  calculation.

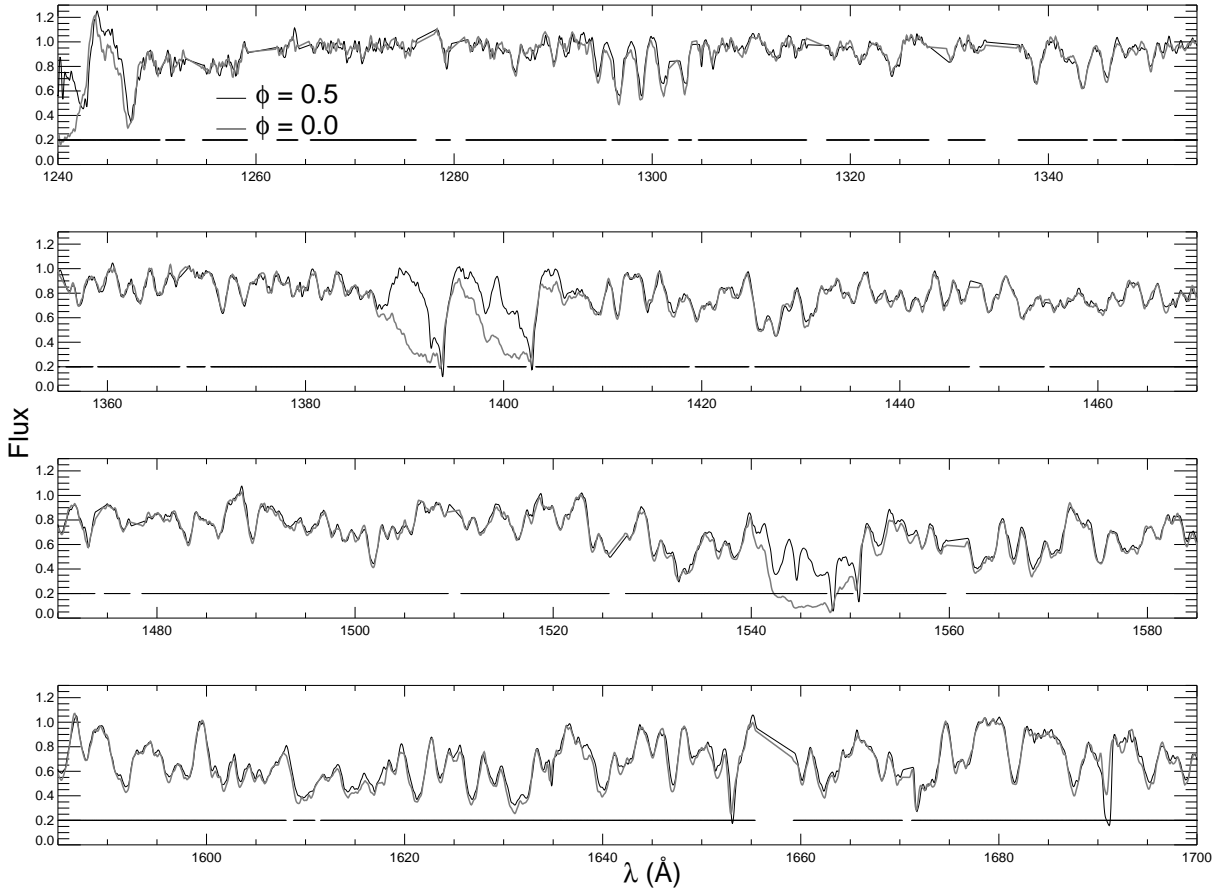


Fig. 5.— Averaged UV spectra of HD 226868 at orbital phases  $\phi = 0.0$  (*light line*) and  $\phi = 0.5$  (*dark line*). The horizontal line indicates those regions without strong ISM features.

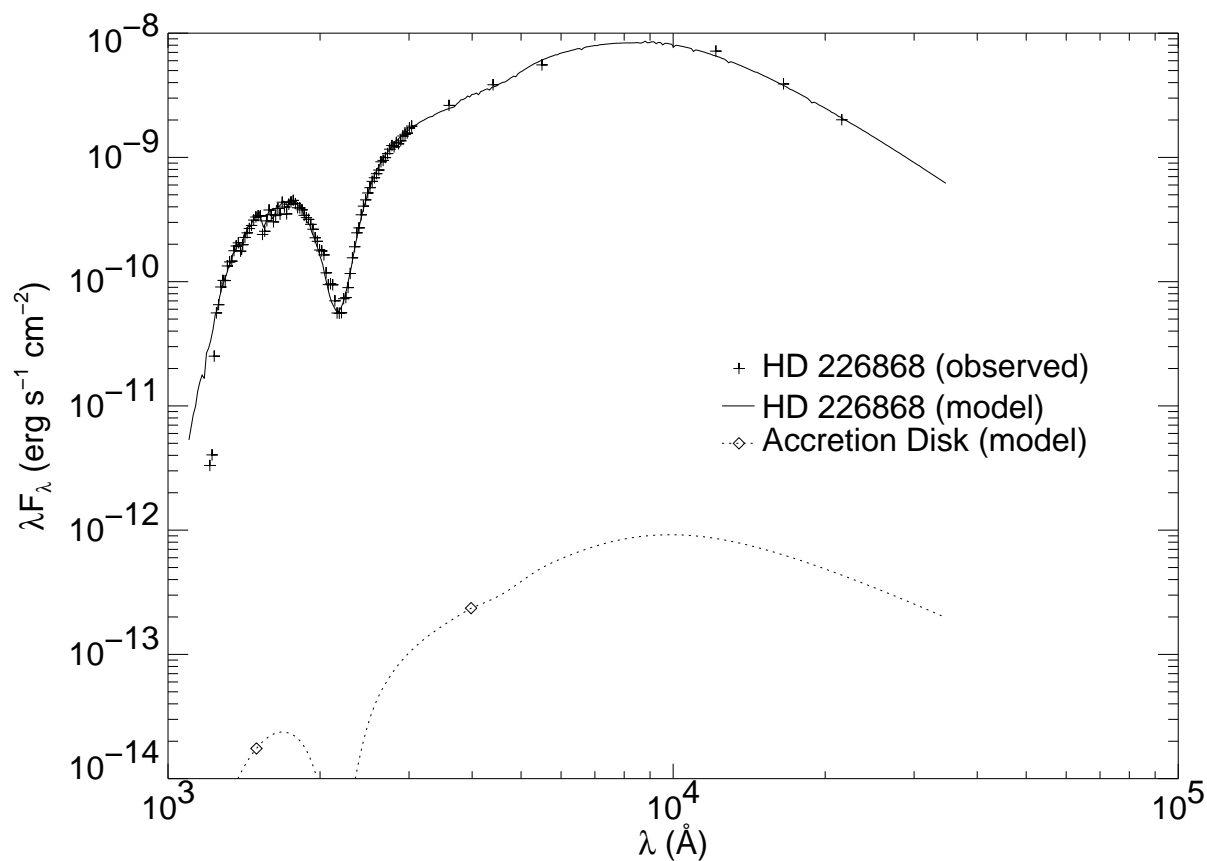


Fig. 6.— The spectral energy distribution of HD 226868 (*plus signs*) together and the TLUSTY best fit (*solid line*) for  $T_{\text{eff}} = 28$  kK and  $\log g = 3.0$ . The UV points were binned from the average *HST* and *IUE* spectra. The three optical points are the *UBV* measurements from Massey et al. (1995) and the three IR points are taken from 2MASS. Also shown is the extrapolation of the accretion disk flux model of Miller et al. (2002) (*dotted line*).

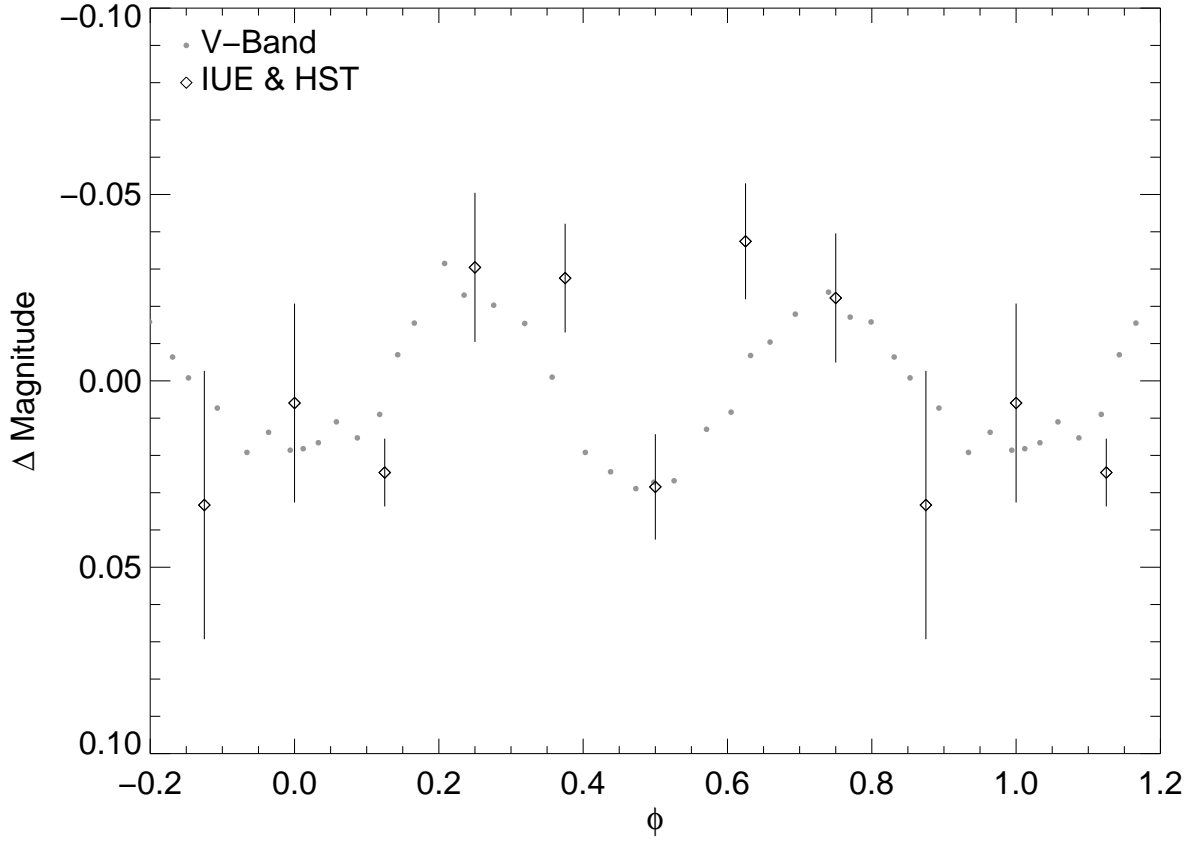


Fig. 7.— UV light curve from both the *HST* and *IUE* spectra (*diamonds*) compared with the *V*-band light curve (*circles*) from Khaliullin & Khaliullina (1981). The UV data were divided into eight orbital phase bins, and the error bars indicate the standard deviation within each bin.

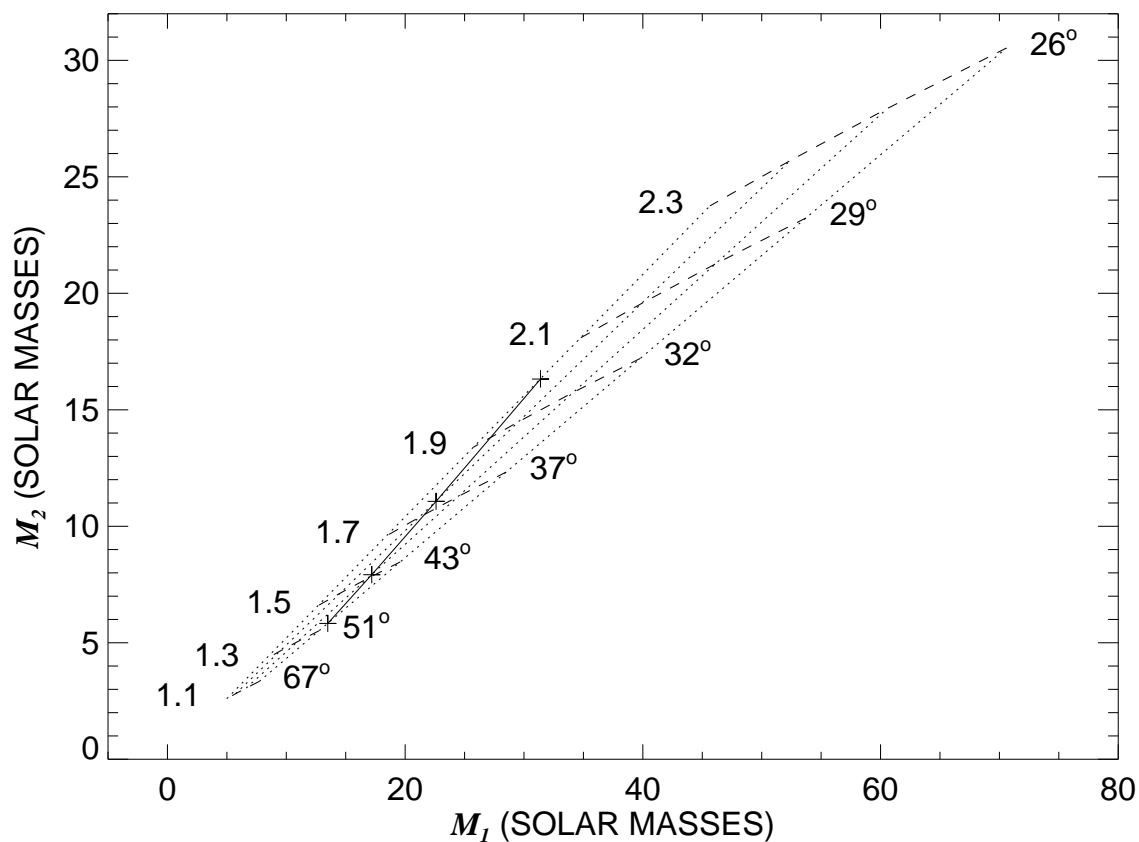


Fig. 8.— Mass plane diagram for the optical ( $x$ -axis) and X-ray ( $y$ -axis) components assuming synchronous rotation of the supergiant. Dotted lines represent fill-out factors ( $\rho$ ) of 0.85 to 1.0 in increments of 0.05 from right-to-left, and the dashed lines show loci of constant distance (in kpc as labeled on the left side while the corresponding orbital inclination rounded to the nearest degree appears on the right side). Plus signs connected by a solid line show the solutions that match the  $V$ -band orbital light curve (Khaliullin & Khaliullina 1981) at each value of the fill-out factor.